Nanoscale Advances

ROYAL SOCIETY OF CHEMISTRY

PAPER

View Article Online
View Journal | View Issue

Cite this: *Nanoscale Adv.*, 2026, **8**, 872

Performance of ultrafine silver chromate particles in electrochemical capacitors for low-pass frequency filtering applications

Pooja Kumari,[a] Mustafizur R. Hazarika,[a] Chandan Saha,[a] Harishchandra Singh[b] and Kaushik Mallick *[a]

Electrochemical capacitors or supercapacitors have become a prominent area of research in energy storage because of their extended cycle life and rapid electrochemical performance along with significant energy and power density. This report provides a comprehensive synthesis and analysis of silver chromate (Ag_2CrO_4) nanoparticles and investigates their electrochemical performance as an electrochemical capacitor. Ag_2CrO_4 is a chemically stable material that exhibits high electrical conductivity and low solubility, making it an ideal candidate for supercapacitor applications. Nanosized Ag_2CrO_4 was synthesized using an organic molecule mediated complexation route where particles ranging from 10 to 30 nm in size are encapsulated within the organic matrix. For the Ag_2CrO_4-based three-electrode system, at a scan rate and current density of 5 mV s^{-1} and 3 A g^{-1}, the specific capacity values obtained were 131 and 203C g^{-1}, respectively. An asymmetric supercapacitor device was fabricated utilizing Ag_2CrO_4 as the cathode and activated carbon as the anode material, which displayed a specific capacity of 36C g^{-1} at 0.4 A g^{-1} and 31C g^{-1} at 10 mV s^{-1}. The assembled device displayed a maximum power density of 361 W kg^{-1} at an energy density of 1.5 Wh kg^{-1}. The performance of the device was successfully demonstrated by powering a red LED, confirming its capability as an energy storage component. Furthermore, the ability of the device to attenuate high-frequency signals was demonstrated through its integration into a resistor–capacitor (RC) circuit, where it operated as a low-pass filter, emphasizing its potential for use in frequency-selective electronic applications.

Received 2nd September 2025
Accepted 30th November 2025

DOI: 10.1039/d5na00843c

rsc.li/nanoscale-advances

Introduction

Supercapacitors have attracted significant research attention as a promising solution for sustainable and renewable energy storage owing to their key properties, such as rapid charge–discharge capabilities, impressive cycle life, high specific power and environment friendly design.[1–3] These attributes make supercapacitors a compelling choice for a variety of applications in energy management and sustainable technology.[4] Researchers are actively exploring strategies to enhance supercapacitor performance by developing advanced materials, with a particular focus on optimizing the electrode material, which plays a critical role in determining the overall effectiveness of the device.

Most commercially used supercapacitors are made of carbon-based electrodes, which offer numerous advantages, including low cost, excellent corrosion resistance, good cycling stability, high electrical conductivity and strong mechanical properties.[5,6] Metal oxides are known for their superior

Scheme 1 Schematic representation of the reaction pathway for the synthesis of silver chromate.

[a]Department of Chemical Sciences, University of Johannesburg, P. O. Box: 524, Auckland Park, 2006, South Africa. E-mail: kaushikm@uj.ac.za
[b]Nano and Molecular Systems Research Unit, University of Oulu, FIN-90014, Finlan

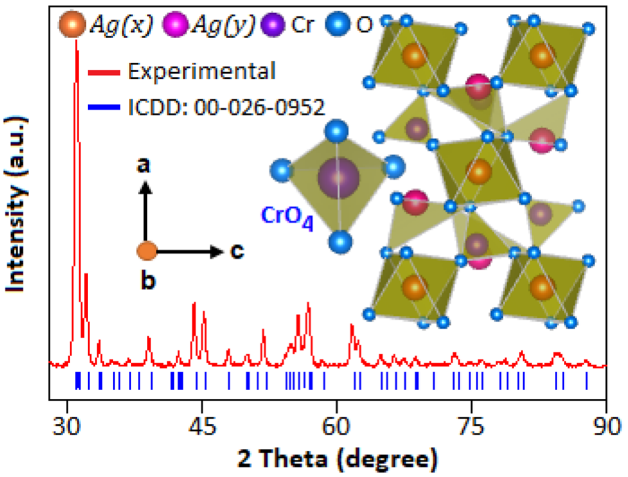

Fig. 1 XRD pattern and unit cell representation of Ag_2CrO_4.

electrochemical properties, offering higher specific capacitance, enhanced chemical stability and greater energy density.[7] Among these, transition metal oxides, such as nickel oxide,[8] manganese oxide,[9] ruthenium dioxide,[10] iridium oxide,[11] cobalt oxide,[12] copper oxide,[13] zinc oxide,[14] chromium oxide,[15] *etc.* stand out as promising candidates for use as electrode materials in electrochemical supercapacitors. These oxides are highly regarded for their ability to store and deliver energy efficiently, making them ideal for advanced supercapacitor applications. However, the primary obstacles associated with transition metal-based electrode materials include their limited specific energy and high internal resistance.[16,17] To provide high specific energy, which is crucial for the performance of supercapacitor devices, the electrodes must also facilitate rapid electron transport to ensure the overall effectiveness of the supercapacitor.[18] To achieve this goal, silver-containing materials have been developed because the reduced product (metallic silver) can form a network that supports fast electron transport.[18]

The energy storage behavior of silver vanadate as a cathode material involves a reversible intercalation–deintercalation process coupled with an irreversible displacement reaction, forming a conductive silver matrix that enhances high rate performance.[19] Silver molybdate (Ag_2MoO_4) nanoparticle based novel electrodes were used to fabricate a high-performance asymmetric supercapacitor device that provided an energy density of 72.1 Wh kg^{-1}.[20] It was reported that mesoporous β-Ag_2MoO_4 as a supercapacitor electrode displayed a specific capacity of 2610C g^{-1} at 1 A g^{-1}.[21]

Among the various silver-based materials, Ag_2CrO_4 stands out as an attractive photocatalyst for the degradation of organic pollutants.[22–24] Despite its promising photocatalytic properties, there are no reports available in the literature regarding the performance of Ag_2CrO_4 as an energy storage material. The exploration of Ag_2CrO_4 for supercapacitor applications is justified by its favorable electronic structure, redox-active nature, and excellent chemical stability, which are crucial characteristics for efficient charge storage. Moreover, materials that exhibit strong photocatalytic activity often possess high surface area and efficient charge separation properties that are also advantageous for supercapacitor electrodes.

In this work, Ag_2CrO_4 nanoparticles were synthesized using silver nitrate and potassium chromate as precursors. The synthesis was carried out through a hexamethylenetetramine mediated complexation route, which enabled the controlled formation of the nanoparticles. The Ag_2CrO_4 nanoparticles, stabilized by an organic molecule, were used as the cathode material in the construction of an asymmetric electrochemical capacitor for energy storage applications. Silver chromate was chosen as the electrode material because of its unique redox activity, excellent electrochemical properties and good electrical conductivity. The ability of the capacitor to attenuate high-frequency signals was evaluated through integration into a resistor–capacitor circuit, demonstrating potential for low-pass filter applications.

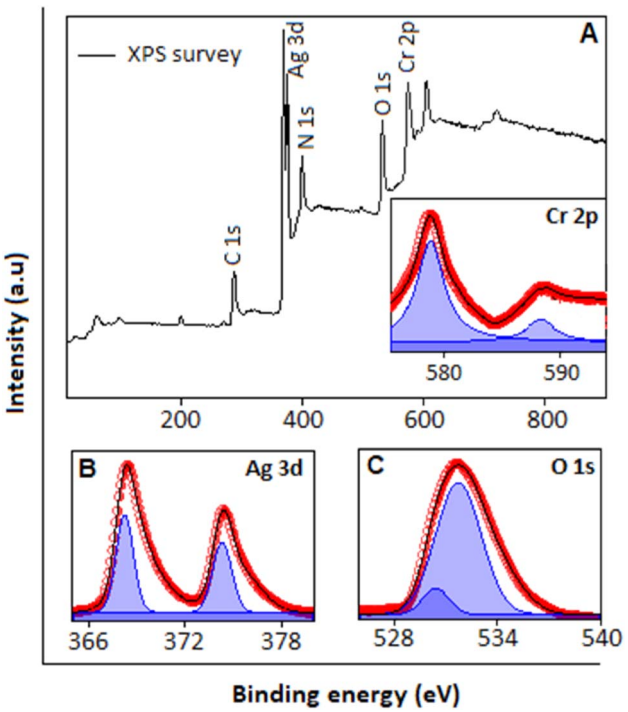

Fig. 2 (A) XPS survey spectrum of Ag_2CrO_4 (main panel). Inset: high-resolution Cr 2p spectrum. High-resolution XPS spectrum of (B) Ag 3d, (C) O 1s, (D) N 1s and (E) C 1s.

Experimental section

Materials

Analytical grade silver nitrate, hexamethylenetetramine (hexamine), potassium hydroxide and potassium chromate were used in this study without additional purification.

Synthesis of Ag_2CrO_4 nanoparticles

To synthesize silver chromate, 0.20 g of hexamine was dissolved in methanol (15 mL), followed by the addition of 7 mL

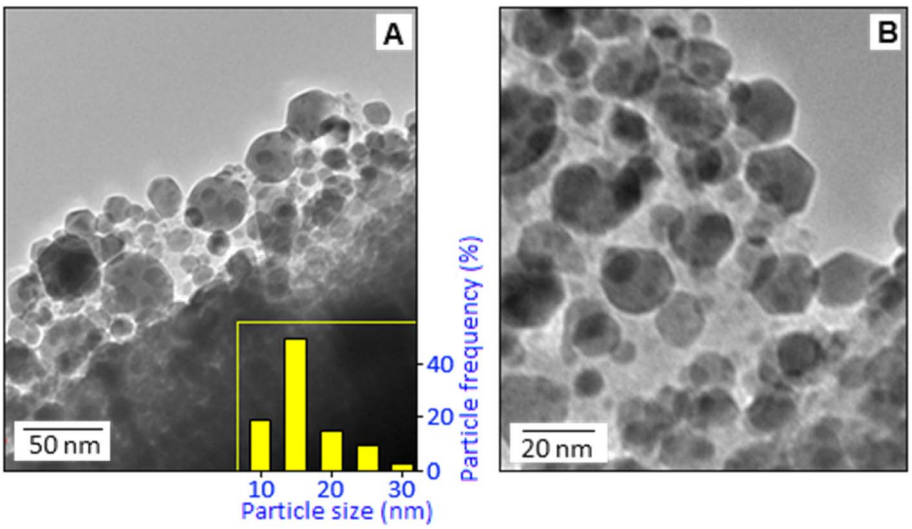

Fig. 3 TEM images (A and B) of Ag_2CrO_4 particles at different magnifications. The inset in figure (A) shows the histogram (particle size as a function of particle frequency).

of 0.1 M aqueous silver nitrate solution, resulting in the formation of a white Ag(I)–hexamine complex as a precipitate. The complex was kept for 3 h without disturbance under ambient conditions. In the next step, the precipitate was subjected to the dropwise addition of 5 mL of 0.1 M potassium chromate solution under stirring, causing the formation of hexamine stabilized silver chromate (dark red colour). A schematic diagram illustrating the synthesis process of silver chromate is presented in Scheme 1, providing a visual overview of the reaction pathway. The solid product was obtained *via* filtration, washed three times with a mixture of deionized water and methanol (1 : 1 ratio), dried under vacuum at 60 °C and characterized using different analytical techniques. The synthesized product was used as an active ingredient (cathode material) for supercapacitor application.

Material characterization

Various characterization techniques were employed to analyse the synthesized material, such as X-ray diffraction (XRD, PANalytical X'pert diffractometer), transmission electron microscopy (TEM, JEOL JEM-2100) and X-ray photoelectron spectroscopy (XPS, Thermo Scientific MultiLab 2000). Nitrogen adsorption–desorption isotherms were measured using a *Quantachrome NOVA 2200E* BET surface area analyzer. Surface features were examined using a JEOL JSM-840 scanning electron microscope (SEM) operating at 15 kV. The electrochemical

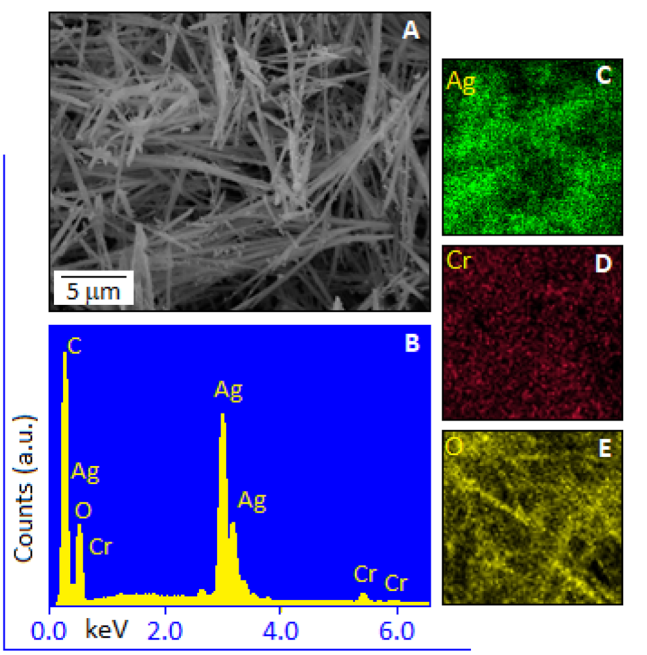

Fig. 4 (A) SEM image of hexamine stabilized Ag_2CrO_4. Energy dispersive X-ray spectra (B) and corresponding element mapping of silver (C), chromium (D) and oxygen (E).

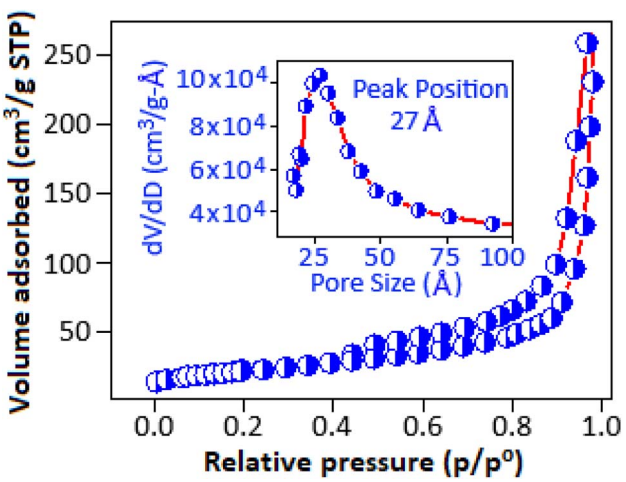

Fig. 5 Nitrogen adsorption–desorption isotherm and the pore size analysis (inset) of the synthesized material (Ag_2CrO_4).

performances were measured utilizing a Bio-Logic SP-200 system.

Fabrication of the three-electrode system and an asymmetric supercapacitor (electrochemical capacitor)

The three-electrode setup comprises a Ni-foam as the working electrode, a calomel ($Hg–Hg_2Cl_2$) electrode as the reference electrode and a Pt-wire as the counter electrode. The electroactive material was prepared, in the form of a slurry, using Ag_2CrO_4, conducting carbon and poly-vinylidene fluoride (PVDF) in a ratio of 8 : 1 : 1 (wt%) in the presence of 10 μL of *N*-methyl pyrrolidine (NMP) and coated onto Ni-foam with a mass loading of 1.2 mg, which was used as the active working electrode. The ASC was assembled in a coin cell configuration. To fabricate the ASC, the as-prepared Ag_2CrO_4 and activated carbon (AC) were used as the cathode and anode, respectively. The cathode electrode material for the device was prepared as described above. The anode electrode was prepared by mixing AC and PVDF (95 : 5 wt%) in NMP. The prepared electrode materials were deposited on two nickel foams and vacuum-dried at 60 °C. The electrodes were then separated using KOH-soaked filter paper and assembled into a CR2032-type coin cell. The mass balance of both the electrodes was calculated using the equation $m_+/m_- = CS_- \times V_-/CS_+ \times V_+$ (CS_+, m_+, V_+ and CS_-, m_-, V_- are the specific capacity, mass and potential window of the cathode and anode electrodes, respectively). The total mass loading of the device was 3.6 mg.

The electrochemical parameters were calculated utilizing the following equations. Specific capacity (CS in C g^{-1}) = $\int I dV/m \times v$ (i) and $\Delta t \times I/m$ (ii), where $\int I dV$ is the area under the cyclic voltammetry (CV) curves and Δt, I, m and v represent the discharge time, current, mass of the electroactive material and scan rate, respectively. Coulombic efficiency (CE) = $(t_d/t_c) \times 100$ (iii), where t_d and t_c are discharging and charging times, respectively. Energy density (ED in Wh kg^{-1}) = $V \times \int I dt/2 \times 3.6 \times m$ (iv) and power density (PD in W kg^{-1}) = $(ED/\Delta t) \times 3600$ (v).

Results and discussion

The mechanism of complexation mediated synthesis of hexamine stabilized Ag_2CrO_4 nanoparticles can be explained as follows. In this work, hexamine (hexamethylenetetramine), a cyclic amine with a cage-like structure, was employed as a complexation agent. Acting as a multidentate ligand, hexamine coordinates to the silver ion through the lone pairs of nitrogen, facilitating the formation of a stable Ag(I)–hexamine

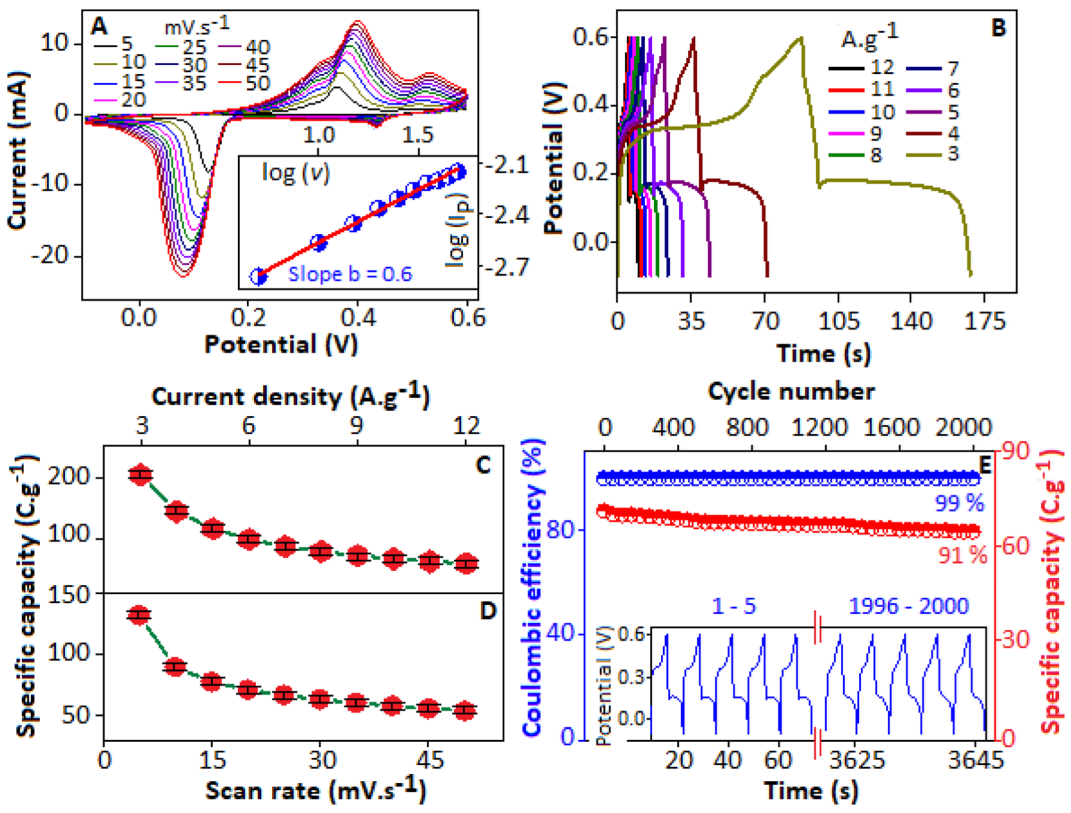

Fig. 6 (A) Cyclic voltammograms of the Ni-foam modified Ag_2CrO_4 based working electrode for the three-electrode system at scan rates of 5–50 mV s^{-1} in the presence of 1 M KOH. Inset: the graphical representation of peak current as a function of scan rate (in log–log scale). (B) Galvanostatic charge–discharge profile at current densities ranging from 12.0 to 3.0 A g^{-1}. Specific capacity as a function of (C) current density (12.0–3.0 A g^{-1}) and (D) scan rates (5–50 mV s^{-1}), repeated three times. (E) Cycling stability for 2000 charge discharge cycles. The inset represents first five (1–5) and last five (1996–2000) cycles.

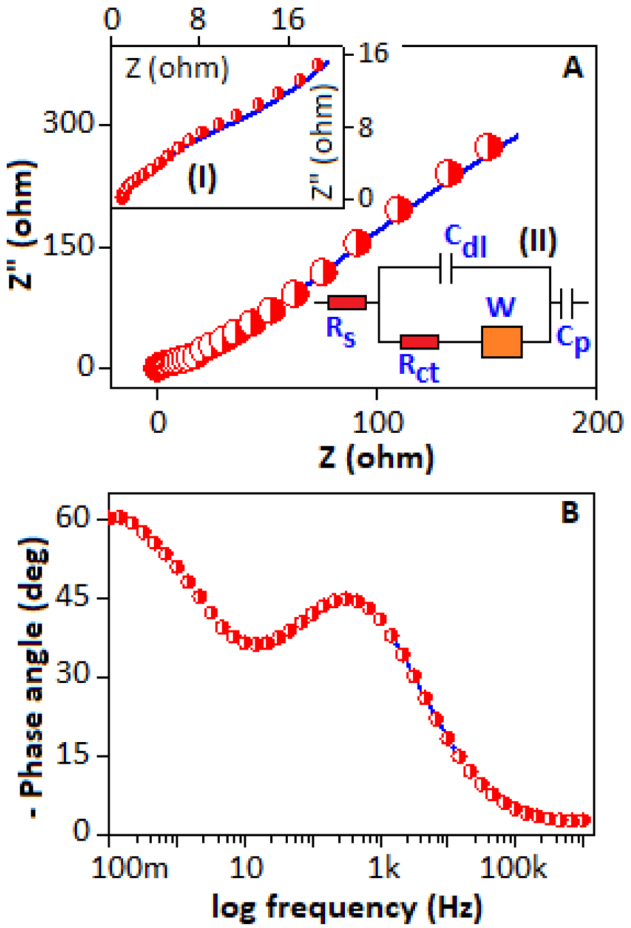

Fig. 7 (A) Nyquist plot measured within the frequency range from 100 mHz to 200 kHz. Inset (I) and (II) show the magnified image of the Nyquist plot for the high frequency region and the equivalent circuit model, respectively. (B) Graphical representation of the phase angle as a function of frequency, Bode plot.

complex. Upon the introduction of aqueous potassium chromate solution, the chromate anion (CrO_4^{2-}) reacted with the silver ions, resulting in the formation of Ag_2CrO_4 particles. The particles were effectively stabilized by the presence of hexamine, which prevents particle agglomeration and controls particle growth.

The XRD analysis of the synthesized material, recorded in the 2θ range of 30° to 90°, Fig. 1, revealed diffraction peaks that matched the JCPDS file 00-026-0952, confirming the formation of Ag_2CrO_4, which corresponds to an orthorhombic crystal structure associated with the space group *Pmnb* (62).[25] The figure shows the unit cell illustration of the Ag_2CrO_4 structure, projected along the *b*-axis, revealing a three-dimensional framework consisting of chromate (CrO_4^{-2}) groups connected with two distinct silver atoms, Ag(*x*) and Ag(*y*). The Ag(*x*) atom adopts a tetragonal bipyramidal geometry, whereas Ag(*y*) is arranged in a distorted tetrahedral configuration with an O–Ag–O bond angle of 107°. The CrO_4^{-2} group also exhibits a distorted tetrahedral structure, characterized by Cr–O bond lengths of 1.66 Å and bond angles ranging from 106.1° to 111.6°. The calculated unit cell parameters are $a = 7.022$ Å, $b = 10.065$ Å, and $c = 5.538$ Å, with $\alpha = \beta = \gamma = 90°$, resulting in a cell volume of ~391.4 Å^3.[26]

XPS analysis was utilized to examine the elemental composition and oxidation states of the synthesized Ag_2CrO_4. The survey spectra, Fig. 2A, display the peaks corresponding to Cr, Ag, O, N and C. The characteristic peaks for nitrogen and carbon originated from the organic molecule (hexamine). The high-resolution Cr 2p spectrum (Fig. 2A, inset) displays two peaks positioned at 588.4 eV and 578.3 eV, corresponding to $2p_{1/2}$ and $2p_{3/2}$, respectively, representing the Cr(VI) oxidation state, which supports the formation of Ag_2CrO_4.[27–29] Fig. 2B shows the high-resolution Ag 3d spectrum with two distinct peaks present at 367.5 eV and 373.3 eV corresponding to the Ag $3d_{5/2}$ and Ag $3d_{3/2}$ states, respectively, which are the characteristic peaks for Ag(I).[23,29] The deconvoluted high resolution O 1s spectrum, Fig. 2C, exhibits peaks at 530.2 and 531.6 eV corresponding to lattice oxygen and the hydroxyl groups adsorbed on the surface of Ag_2CrO_4, respectively.[30,31]

Transmission electron microscopy images, Fig. 3(A and B), reveal that the silver chromate nanoparticles are predominantly spherical in shape with a broad size distribution. The particles are moderately well-dispersed, although some degree of aggregation is noticeable, which is common in nanoscale systems due to high surface energy. The histogram, Fig. 3A, inset, shows the particle size distribution, indicating that most of the nanoparticles fall within the range of 10–30 nm. A small fraction of the particles also exhibits a hexagonal shape, as observed in Fig. 3B, highlighted within a circle. Fig. 4A, shows the scanning electron microscopy image of the Ag_2CrO_4 based hybrid system. The image highlights the surface morphology of the system at a microscopic level. Elemental analysis using the energy dispersive X-ray spectroscopy technique shows the presence of Ag, Cr and O in the sample, Fig. 4B. The elemental mapping shows uniform distributions of Ag, Cr and O in Ag_2CrO_4, Fig. 4(C–E). The elemental mapping also ensures that Ag, Cr and O are well-integrated at a microscopic level.

The nitrogen adsorption–desorption isotherm of Ag_2CrO_4 is shown in Fig. 5. Based on IUPAC classification, the isotherm is classified as type IV, featuring a distinct H1 hysteresis loop between relative pressures of 0.4 and 1.0. The surface area, measured by the Brunauer–Emmett–Teller (BET) technique, was calculated to be 72.7 m^2 g^{-1}. Further analysis using the Barrett–Joyner–Halenda (BJH) method indicated a maximum pore volume of 0.035 cm^3 g^{-1} and pore diameters distributed within the range of 19–64 Å.

Electrochemical performance of the three-electrode system

The electrochemical behaviour of the Ag_2CrO_4 modified Ni-foam electrode was studied using CV in KOH (1 M) within the voltage range between −0.1 and 0.6 V at various scan rates from 5 to 50 mV s^{-1}. In the CV curve, the absence of a rectangular pattern suggests non-ideal capacitive behaviour of the electrode. The voltammograms, Fig. 6A, demonstrate multiple redox peaks, indicating that the charge storage process is due to a faradaic reaction, which confirms battery-like behaviour

and accounts for a quasi–reversible reaction mechanism.[32] The peaks correspond to the reversible redox process of Cr(VI) ↔ Cr(IV) and Ag(I) ↔ Ag(II) with the intercalation and deintercalation of OH^- ions, attributed to the following reactions:

$$CrO_4^{2-} + 2H_2O + 2e^- \leftrightarrow CrO_2 + 4OH^- \quad (I)$$

$$Ag^+ + 2OH^- \leftrightarrow AgO + 2H_2O + e^- \quad (II)$$

$$2AgO + 2H_2O + 2e^- \leftrightarrow Ag_2O + 2OH^- \quad (III)$$

In the CV curves, Fig. 6A, the redox peak currents increase gradually with increasing scan rate, indicating excellent rate performance and kinetic reversibility.[33] It is also important to mention that with increasing scan rate, the oxidation and reduction peaks shift toward higher and lower potential regions, respectively. The above phenomena are an indication of electrode polarization and an increase in internal diffusion resistance.[33,34] In the voltammogram, it is observed that the curve area is larger at higher scan rates due to the reaction of hydroxyl ions with the surface of the active material. Conversely, at lower scan rates, the curve area decreases as the hydroxyl ions interact with the inner active sites of the electrode material.[35] From the CV study, the CS values were found to be 53C g^{-1} at 50 mV s^{-1} and 131C g^{-1} at 5 mV s^{-1}, calculated using eqn (i).

Nitrogen adsorption–desorption analysis was performed to interpret the electrochemical behavior of the Ag_2CrO_4-modified electrode and its correlation with ion transport kinetics. The electrode material exhibited a moderately high surface area of 72.7 m^2 g^{-1} with a pore size distribution in the range of 19 to 64 Å. These features are crucial for charge storage, where the high surface area provides electroactive sites for faradaic reactions, while the mesoporous structure creates efficient ion-diffusion pathways that reduce resistance and allow deeper access to internal active sites, particularly at low scan rates. The combined electrochemical and BET results confirm that hierarchical porosity facilitates smooth intercalation and deintercalation of electrolyte ions, improving ion accessibility and resulting in higher capacitance.

The electrochemical kinetics of the free-standing electrode were examined using Dunn's method, which evaluated the charge storage performance of Ag_2CrO_4 through both surface-controlled (capacitive contribution) and diffusion-controlled processes. We have applied the power-law equation, $I_p = av^b$, (a is a variable parameter, b is an indicator to evaluate the charge storage kinetics, v and I_p are the scan rate and peak current, respectively) to examine the diffusive and capacitive contributions from the CV data at scan rates from 5.0 to 50 mV s^{-1}.[36] The calculated b-value of 0.6, Fig. 6A, inset, demonstrates

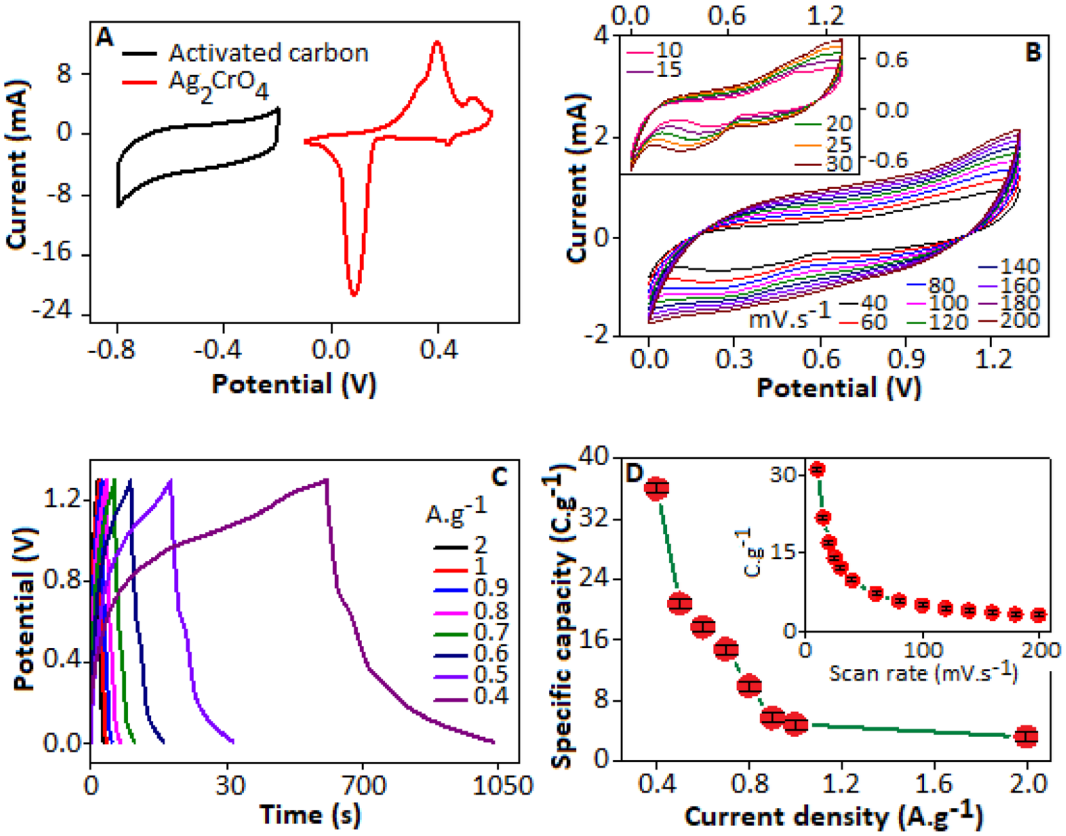

Fig. 8 (A) Comparative cyclic voltammogram of the activated carbon and Ag_2CrO_4 at 40 mV s^{-1}. (B) Cyclic voltammogram of the device at scan rates of 40–200 mV s^{-1} (main panel) and 10–30 mV s^{-1} (inset). (C) Charge–discharge profile of the device at a current density of 2.0–0.4 A g^{-1}. (D) Main panel: specific capacity as a function of current density (2.0–0.4 A g^{-1}). Inset: specific capacity as a function of scan rate (10–200 mV s^{-1}), repeated three times.

that the diffusion-controlled process dominates the charge-storage mechanism.

The GCD profile, Fig. 6B, of the Ag_2CrO_4 modified electrode was studied within the potential window of −0.1 to 0.6 V at various current densities (CDs) from 12–3 A g^{-1}. The nonlinear nature of the charge–discharge curves indicates that the storage (energy) mechanism is predominantly associated with the electrochemical oxidation–reduction process, similar to battery-type electrodes. The appearance of a potential drop in the discharge curve along with a sudden potential increase is due to a quasi–conversion reaction, an inherent electrochemical behaviour of the silver-based materials. The CS values obtained from charge–discharge curves were 59 and 203C g^{-1}, at CD values of 12 and 3 A g^{-1}, respectively, calculated using equation (ii).

The dependence of CS on CD and scan rate is demonstrated in Fig. 6(C and D). The electrode was stable and showed high reproducibility across three batches with a standard deviation below 3%. This trend can be attributed to the limited time available for charge carriers to participate in redox reactions at higher rates, leading to incomplete utilization of the active material and hindering the efficiency of faradaic charge storage processes. The aforementioned factors contribute to the observed reduction in specific capacity under high-rate operating conditions. The cycling stability of the electrode is an important characteristic for real time applications. In this case, the GCD study was applied to evaluate the long-term stability of the electrode. At a CD of 9 A g^{-1}, the Ag_2CrO_4 electrode showed a capacity retention and CE of 91% and 99%, respectively, after 2000 cycles, Fig. 6E. The inset figure displays the first five (1–5) and last five (1996–2000) charge–discharge cycles. The electrode exhibited high reproducibility with a standard deviation below 4% for three consecutive batches. We further performed X-ray diffraction (XRD) analysis, Fig. S1, SI, after completing the galvanostatic charge–discharge cycles. The obtained XRD pattern did not show any noticeable shift or emergence of new diffraction peaks, indicating that the crystalline phase of the electrode material remained unchanged. This observation confirms the structural stability and robustness of the electrode material during repeated electrochemical cycling.

The impedance spectroscopy study was carried out across a frequency range of 100 mHz–200 kHz. The expanded view of the high frequency region of the Nyquist plot is displayed in Fig. 7A, inset (I). The Nyquist data of the device were fitted with the equivalent circuit model (Randle circuit), inset (II), consisting of solution resistance (R_S), double layer capacitance (C_{dl}), charge transfer resistance (R_{ct}) and Warburg impedance (W). The low-frequency and high-frequency regions indicate the ion diffusion mechanism and charge transfer process, respectively. The R_S and R_{ct} values were 0.96 Ω and 2.83 Ω, respectively, obtained from the fitting curve. The Bode plot, Fig. 7B, of the Ag_2CrO_4 based electrode shows the intercept at low frequency with a phase angle of −60°, which indicates efficient charge storage performance and quick ion diffusion.[37,38] The plot also shows a prominent peak (time constant)

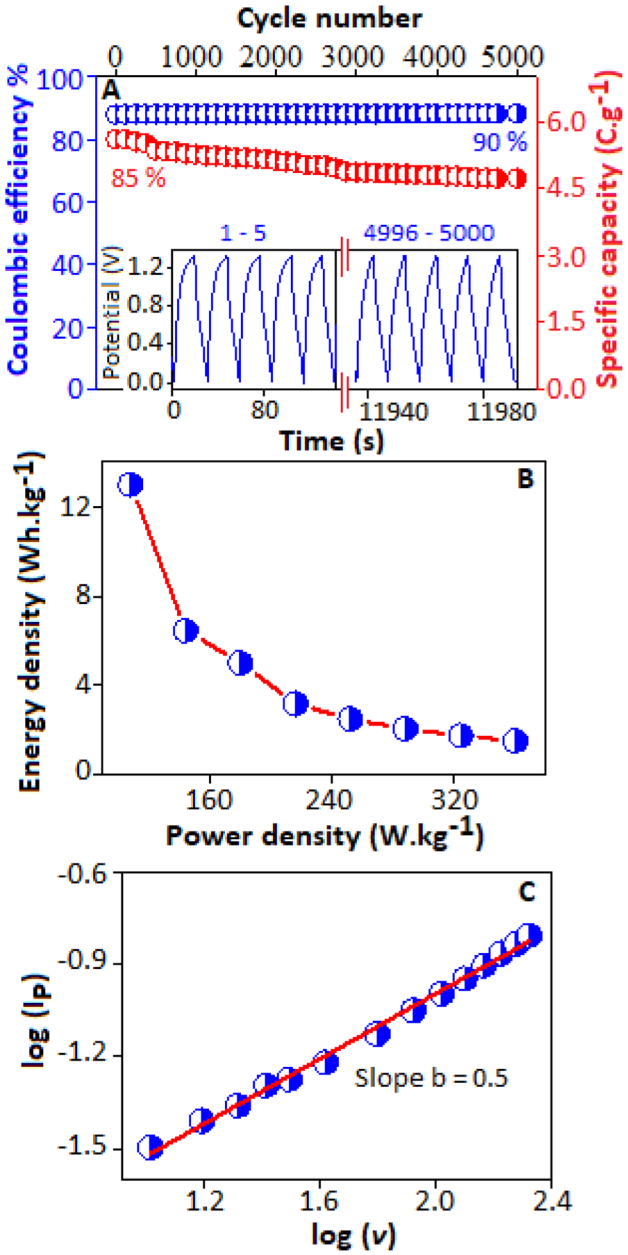

Fig. 9 (A) Cycling stability over 5000 charge–discharge cycles. The inset represents first five (1–5) and last five (4996–5000) cycles. (B) Energy density as a function of power density of the asymmetric device. (C) Graphical representation of peak current as a function of scan rate (log–log scale).

at 37 Hz, indicating the behaviour of double layer capacitance.[39]

Electrochemical performance of the asymmetric capacitor

To assess the practical application of Ag_2CrO_4, an ASC device was assembled using Ag_2CrO_4 as the cathode and AC as the anode. The advantage of an asymmetric supercapacitor over a symmetric one is that the asymmetric device leverages the different voltage windows of the cathode and anode electrodes, enabling it to operate efficiently in a higher potential

Table 1 A comparative table based on the electrochemical performance of some chromium-based materials[a]

Electrode material (*)	Electrolyte (M)	Three- electrode	Two-electrode (SC device)	Energy density	Power density	Retention (%) and cycle number	Ref.
CrO_XN_Y	KOH (3)	105 F g^{-1} @ 1 A g^{-1}	146 F g^{-1} @ 5 mV s^{-1} (symmetric)	8 Wh kg^{-1}	28.8 kW kg^{-1}	98% @ 10 000	40
MIL-101(Cr, Mg)-rGO	KOH (6)	261.4 F g^{-1} @ 1 A g^{-1}	—	4.6 Wh kg^{-1}	7.6 kW kg^{-1}	86% @ 2000	41
Co–Cr-LDH	KOH (2)	732C g^{-1} @ 1 A g^{-1}	148.5 F g^{-1} @ 0.8 A g^{-1} (asymmetric)	35.1 Wh kg^{-1}	1.2 kW kg^{-1}	90% @ 5000	42
$(Fe, Cr)_2O_3$	KOH (1)	45.9 mF cm^{-2} @ 5 mV s^{-1}	16.8 mF cm^{-2} @ 5 mV s^{-1} (symmetric)	0.57 mWh cm^{-2}	200 mW cm^{-2}	115% @ 5000	43
Ni_2Cr_1-LDNs	KOH (6)	1525 F g^{-1} @ 2 A g^{-1}	155 F g^{-1} @ 0.5 A g^{-1} (asymmetric)	55.33 Wh kg^{-1}	400 W kg^{-1}	81% @ 5000	44
$NiCrO_3$	KOH (6)	2862 F g^{-1} @ 1 A g^{-1}	102.7 F g^{-1} @ 2 A g^{-1} (asymmetric)	32.9 Wh kg^{-1}	1.5 kW kg^{-1}	48% @ 50 000	45
$CoCr_2O_4$	Na_2SO_4 (1)	883 F g^{-1} @ 5 mV s^{-1}	74 F g^{-1} @ 0.5 A g^{-1} (asymmetric)	26.3 Wh kg^{-1}	400 W kg^{-1}	91% @ 5000	46
Cr_2O_3	KOH (2)	300 F g^{-1} @ 1 mV s^{-1}	50 F g^{-1} @ 1.0 A g^{-1} (asymmetric)	14.2 Wh kg^{-1}	568.2 W kg^{-1}	98% @ 3000	47
Cr_2O_3	KOH (6)	453 F g^{-1} @ 1 A g^{-1}	79 F g^{-1} @ 1 A g^{-1} (symmetric)	15.8 Wh kg^{-1}	600.5 W kg^{-1}	90% @ 5000	48
Cr_2O_3–Co_3O_4 NC	KOH (1)	619.4 F g^{-1} @ 10 mV s^{-1}	33.07 F g^{-1} @ 10 mV s^{-1} (asymmetric)	4.3 Wh kg^{-1}	200 W kg^{-1}	74.8% @ 1000	49
Cr_2O_3–MoO_2	Na_2SO_4 (1)	340 F g^{-1} @ 2 mA cm^{-2}	74.5 F g^{-1} @2 mA cm^{-2} (asymmetric)	37.35 Wh kg^{-1}	9708 W kg^{-1}	91% @ 20 000	50
Ag_2CrO_4	KOH (1)	203C g^{-1} @ 3 A g^{-1}	36C g^{-1} @ 0.4 A g^{-1} (asymmetric)	13 Wh kg^{-1}	361 W kg^{-1}	85% @ 5000	This work

[a] (*) CrO_XN_Y: chromium oxynitride; MIL-101(Cr, Mg)-rGO: Mg-doped chromium-based metal organic framework-reduced graphene oxide composite; Co–Cr-LDH: 2-D cobalt-chromium layered double hydroxide and poly-oxo-vanadate anions; Ni_2Cr_1-LDNs: nickel-chromium layered double hydroxide nanoflakes. $CoCr_2O_4$: cobalt chromite; Cr_2O_3: chromium oxide; Cr_2O_3–Co_3O_4 NC: chromium oxide-cobalt oxide-based nanocomposite; Cr_2O_3–MoO_2: chromium oxide–molybdenum dioxide.

window. To achieve optimum performance of the device, a charge-to-mass balance should be performed between both the electrodes. The calculated mass ratio (m_+/m_-) was 0.5, considering the capacities of Ag_2CrO_4 and AC. Fig. 8A shows the comparative CV pattern of Ag_2CrO_4 (−0.1 to 0.6 V) and AC (−0.8 to −0.2 V) at 40 mV s^{-1}. Fig. 8B shows the electrochemical behaviour of the assembled device with a potential window of 1.3 V, $\Delta V_{device} = \Delta V_{positive}$ (0.7 V) + $\Delta V_{negative}$ (0.6 V), at a scan rate between 40–200 mV s^{-1} (main panel) and 10–30 mV s^{-1} (inset). At 10 mV s^{-1}, a maximum CS value of 31C g^{-1} was obtained. The GCD study was performed at various CDs, ranging from 2.0 to 0.4 A g^{-1}, Fig. 8C. The GCD curves validate that the electrochemical performance follows a faradaic process. At a CD of 0.4 A g^{-1}, the device displays a maximum CS of 36C g^{-1}. Fig. 8D displays the CS of the device as a function of CD (main panel) and scan rate (inset), obtained from GCD and CV profiles, respectively. The device was stable and showed high reproducibility across three batches with a standard deviation of approximately 2%. The durability of the device was tested for 5000 charge–discharge cycles at 2 A g^{-1}. Fig. 9A (main panel) displays the CE and CS for each charge–discharge cycle. The results suggest that the device retains 85% of the initial capacity and ∼90% of coulombic efficiency after 5000 cycles. The inset figure displays the first five (1–5) and last five (4996–5000) charge–discharge cycles. The device exhibited high reproducibility across three batches, with a standard deviation below 4%. The observed capacity fading mechanism is attributed to several interrelated factors, including structural distortion of the electrode material, partial dissolution of the active material into the electrolyte and the gradual buildup of internal resistance caused by the deterioration of the electrode–electrolyte interface over repeated charge–discharge cycles. Supercapacitors are characterized by two significant parameters *i.e.*, ED and PD, calculated using equations (iv) and (v). For the current device, a maximum PD of 361 W kg^{-1} was obtained at an ED of 1.5 Wh kg^{-1}. Fig. 9B shows the ED *versus* PD variation (Ragone plot) for the device. A comparative overview of the electrochemical performance of some chromium-based materials is provided in Table 1 as a ready reference.[40–50]

Furthermore, to enhance the performance of such capacitors, several effective strategies can be implemented. These include optimizing the electrode surface area to maximize the number of active sites, incorporating conductive additives to enhance electron transport pathways, and refining the synthesis methodology by altering the complexation agent to control the morphology and increase the pore size of the active material, thereby facilitating efficient ion diffusion. In addition, employing redox-active or multi-electrolyte systems can further improve the charge storage capability, resulting in a significant boost in specific capacitance, energy density and long-term cycling stability of the device.

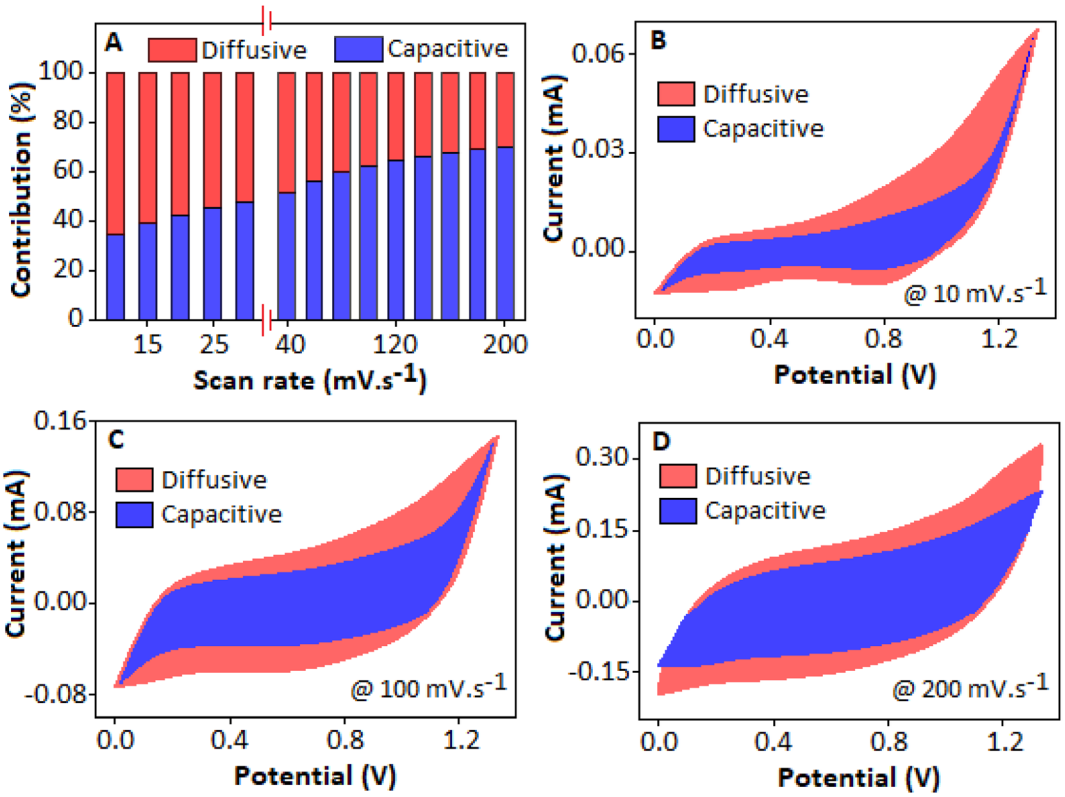

Fig. 10 (A) Bar diagram for the capacitive and diffusive contributions of the device at different scan rates from 10 mV s^{-1} to 200 mV s^{-1}. (B–D) Capacitive and diffusion contributions based on the experimental CV curves at 10, 100 and 200 mV s^{-1} respectively.

We further calculated the total charge storage mechanism of the device using the power law equation, $I_p = av^b$,[51] which can be derived as $\log(I_p) = \log(av^b) = \log(a) + b\log(v)$. The slope of the $\log(I_p)$ *vs.* $\log(v)$ plot defines the *b*-value, which is 0.5, Fig. 9C, validating the diffusion controlled charge storage mechanism. The capacitive and diffusion-controlled contributions to the total capacity at a given potential at each scan rate were further evaluated using the equation $I_p = k_1v + k_2v^{1/2}$, where k_1v and $k_2v^{1/2}$ represent capacitive (surface-controlled) and diffusion controlled processes, respectively. The above equation can be rearranged as, $I_p/v^{1/2} = k_1v^{1/2} + k_2$. The values of k_1 and k_2 can be obtained by plotting $I_p/v^{1/2}$ *vs.* $v^{1/2}$. The Ag_2CrO_4-based device displayed a surface-controlled capacitive contribution of 34% at 10 mV s^{-1}, which increased to 70% at 200 mV s^{-1}, Fig. 10A. At lower scan rates, the majority of ions in the device remain on the outer surface of the electrode, with ion diffusion behaviour dominating over the capacitive contribution. As the scan rate increased, the device exhibited a steady rise in capacitive contribution, which is advantageous for achieving high power density.[52] Fig. 10(B–D) illustrates the cyclic voltammograms of the Ag_2CrO_4 based device at 10, 100 and 200 mV s^{-1}. The red shaded area represents the diffusion controlled contribution and the blue shaded area of the curve represents capacitive controlled contribution.

The pattern of the Nyquist plot for the free-standing electrode and device are almost identical across the frequency range between 100 mHz and 200 kHz, Fig. 11A. The magnified image of the high-frequency region (semicircle pattern) is shown in Fig. 11A, inset (I). The R_S and R_{ct} values are 2.25 Ω and 9.47 Ω, respectively, obtained from the intercept and diameter of the semicircle. All the fitting parameters are mentioned within the figure, obtained from the Randles circuit, Fig. 11A, inset (II). Fig. 11B, main panel, shows the relationship between imaginary, $C''(\omega)$, and real, $C'(\omega)$, capacitance as a function of frequency. The imaginary and real capacitances are determined from the equations $Z'(\omega) = 2\pi fC''(\omega)|Z(\omega)|$ and $Z''(\omega) = 2\pi fC'(\omega)|Z(\omega)|$, respectively, where ω is the angular frequency, f is the frequency and Z represents the impedance.[53] The real capacitance (C') denotes the available capacitance that can be supplied to the device, which is 0.3 mF. The graphical representation of C'' *vs.* frequency reveals a peak at 1.03 Hz with a relaxation time ($\tau = 1/f$) of 0.15 s, which identifies the time to charge the device. For practical application, two fabricated asymmetric supercapacitor devices (C1 and C2) were connected in series to power a red LED (light emitting diode). It was observed that after being charged for 30 seconds at an applied voltage of 2.6 V and a current density of 0.6 A g^{-1}, the assembled device was capable of powering a red LED for approximately 120 seconds (Fig. 11C). This practical demonstration highlights the ability of the device to store and deliver energy for real-world applications, reflecting its potential for use in low-power electronic systems and backup energy sources.

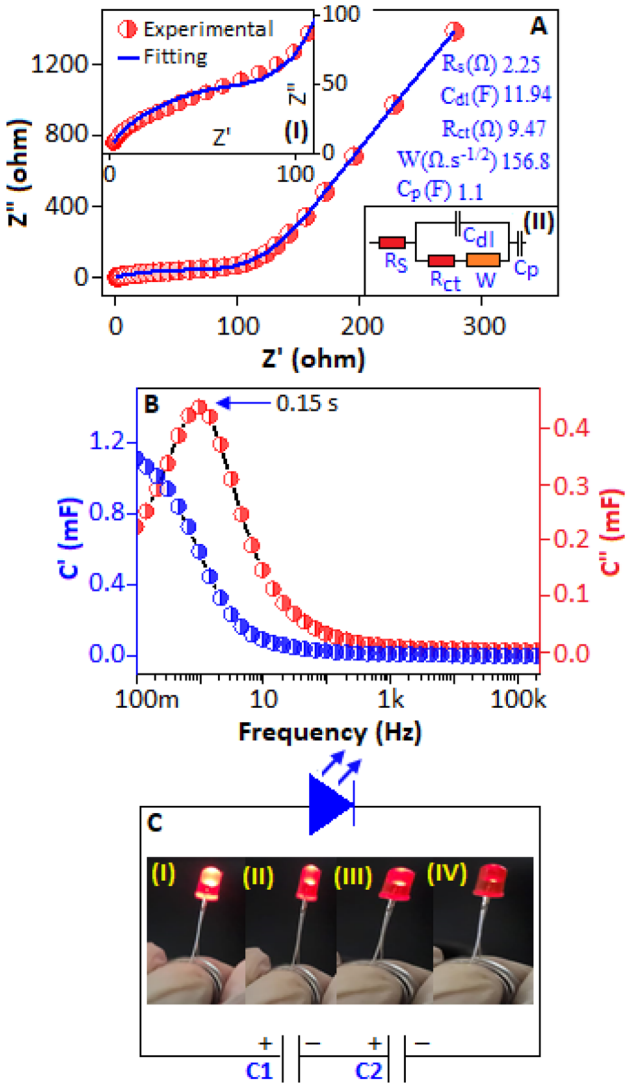

Fig. 11 (A) Nyquist plot measured within the frequency range of 100 mHz to 200 kHz for the device. Inset (I) and (II) show the magnified image of the Nyquist plot for the high frequency region and equivalent circuit model, respectively. (B) The real and the imaginary capacitance as a function of frequency for the device. (C) Photograph of a red LED, at different stages, powered by the Ag_2CrO_4 based two asymmetric devices.

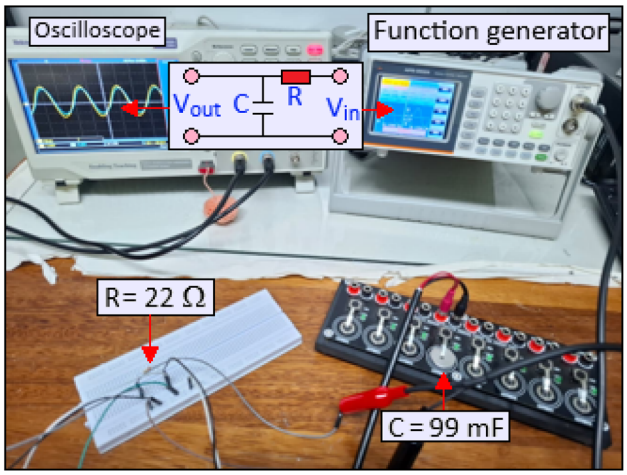

Fig. 12 Experimental setup of the circuit (main panel) and the circuit diagram of the RC low pass filter (inset).

Performance of silver chromate-based electrochemical capacitors in low pass filter applications

A low-pass filter transmits signals below a defined cut-off frequency while attenuating higher-frequency components. The experimental setup, Fig. 12, main panel, and the circuit diagram, Fig. 12, inset, of the low-pass filter were designed by connecting a resistor (R) with a resistance value of 22 Ω and a capacitor (C) with the capacitance value of 99 mF, in series.[54] The resistor provides the load and output impedance, whereas the capacitor introduces frequency-dependent impedance, essential for filtering. The capacitance value was selected based on device performance at a current density of 0.4 A g^{-1} in the silver chromate-based device. The time constant ($\tau = RC'$) represents the rate at which the capacitor charges and discharges within the circuit, which is 22 Ω × 99 mF = 2.178 s, and inversely proportional to the cut-off frequency, $f_c = 1/2\pi RC'$ = 0.07 Hz. The low cut-off frequency results from the high capacitance of the capacitor and the chosen resistor values, $f_c = 1/2\pi RC$, which together determine the RC time constant ($\tau = R \times C$). This large time constant allows probing of the slow charge–discharge behaviour and response of the device. For practical electronic applications requiring higher-frequency operation, the RC time constant can be reduced by selecting smaller resistor values, thereby increasing the cut-off frequency to the desired range while maintaining effective filtering performance. In biomedical instrumentation, such as electrocardiography and electromyography amplifiers, the low cut-off frequency (0.05–0.5 Hz) allows slow physiological signals to pass while blocking DC offsets from electrodes. The performance of the filter was evaluated through MATLAB simulations and hardware implementation, Fig. 13, using an input signal (V_{in}) of 1.2 V_{pp} with input frequency signal values of 0.02, 0.07 and 0.2 Hz. At 0.02 Hz (below cut-off frequency), the capacitor was almost fully charged and discharged in each cycle, and the output waveform (V_{out}) closely follows the input signal. At 0.07 Hz (at the cut-off frequency), incomplete charging–discharging produced amplitude reduction and a noticeable phase lag. The output waveform amplitude decreased by 69.78%, closely matching the simulated output signal drop to 70.7% of the input amplitude, corresponding to −3 dB attenuation.[55] At 0.2 Hz (above the cut-off frequency), the output waveform exhibited strong attenuation, preventing the higher frequency components of the input signal to pass through. The circuit connected with the silver chromate-based capacitor, effectively preserved low-frequency signals and attenuated higher-frequency components, demonstrating its performance as an ideal low-pass filter. A comparative table based on the simulated and experimental output peak voltage values has been included in the manuscript to serve as a ready reference for the readership, Table 2.

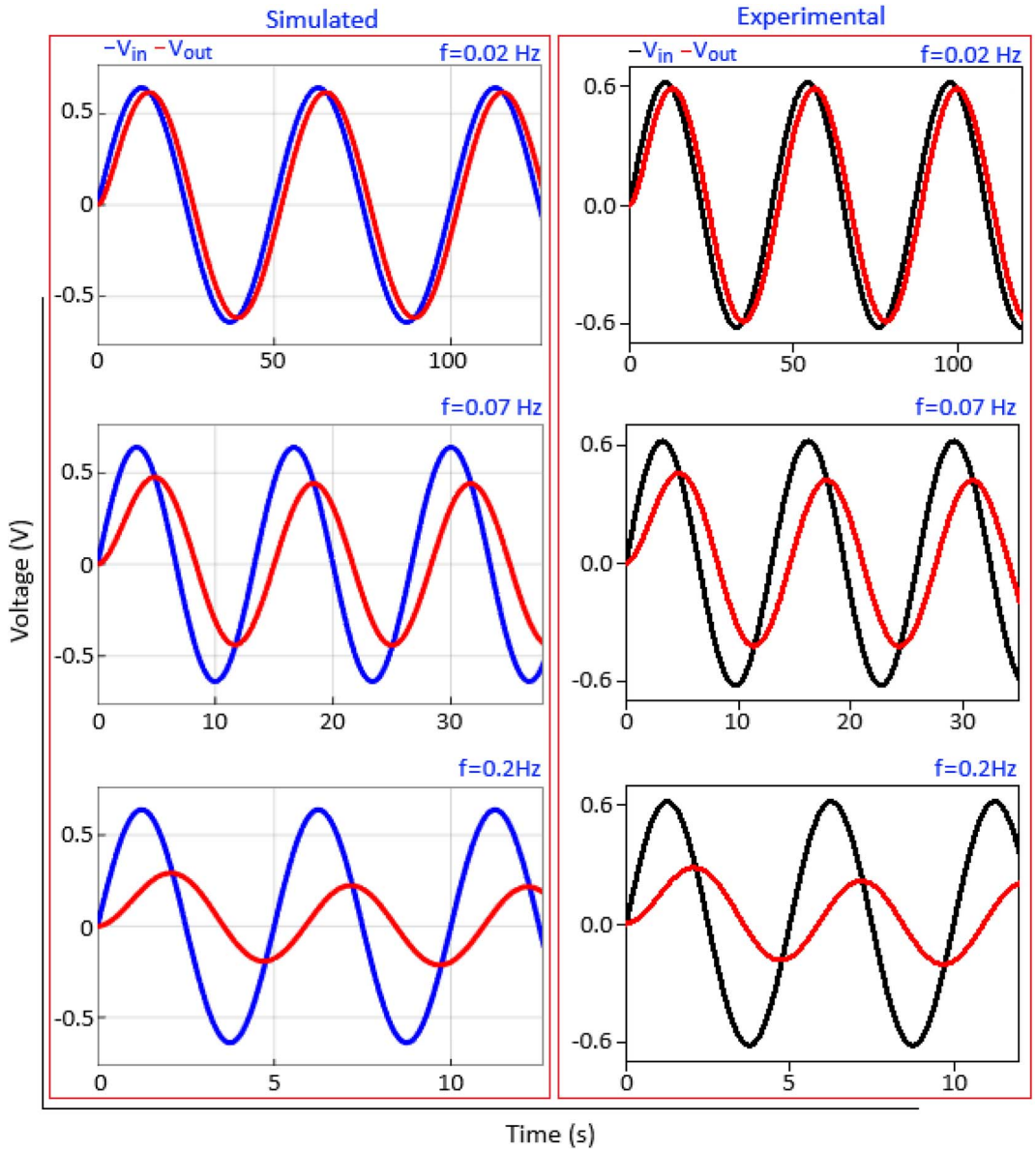

Fig. 13 Simulated and experimental waveforms at frequencies, $f = 0.02$ Hz, 0.07 Hz and 0.2 Hz.

Table 2 Comparison between simulated and experimental voltage output peaks

Frequency (Hz)	Simulated $V_{out\text{-}peak}$ (V)	Experimental $V_{out\text{-}peak}$ (V)	Deviation (%)
0.02	0.59	0.58	1.72
0.07	0.44	0.43	2.33
0.2	0.24	0.23	4.35

Conclusion

Hexamine-stabilized silver chromate nanoparticles, ranging from 10 to 30 nm in size, were synthesized using a complexation-mediated technique. The X-ray diffraction pattern confirms the formation of Ag_2CrO_4, which belongs to the *Pmnb* (62) space group. The unit cell representation highlights a three-dimensional framework consisting of chromate groups linked through two independent silver atoms. The synthesized Ag_2CrO_4 nanoparticles were evaluated for their potential in supercapacitor applications. For the Ag_2CrO_4-based three-electrode system, the specific capacity values of 131 and 203C g^{-1} were obtained at 5 mV s^{-1} and 3 A g^{-1}, respectively. An asymmetric supercapacitor device was fabricated using Ag_2CrO_4 as the cathode and activated carbon as the anode electrode. The device demonstrated specific capacities of 36 and 31C g^{-1} at 0.4 A g^{-1} and 10 mV s^{-1}, highlighting its potential as a cathode material for energy storage applications. The cycling stability of the asymmetric supercapacitor device was tested for 5000 charge–discharge cycles at 2 A g^{-1}, showing 85% retention of its initial specific capacity and 90% of coulombic efficiency, indicating high durability of the system. The fabricated device was

also successfully used to light up a red LED, demonstrating its potential for real-life applications and highlighting its practical viability in energy conversion. The RC circuit incorporating the silver chromate-based capacitor effectively preserved low-frequency signals while attenuating higher-frequency components, thereby demonstrating its functionality as a highly efficient low-pass filter, an essential component in applications such as audio signal processing and noise reduction in communication systems.

Author contributions

PK: conceptualization, experimental work, data curation, writing; MR: simulation and experimental work; CS: material characterization; HS: material characterization, XPS analysis; KM: conceptualization, supervising, funding, review and editing.

Conflicts of interest

The authors declare no conflict of interest.

Data availability

The data supporting the findings of this study will be made available upon reasonable request. Supplementary information (SI) is available. See DOI: https://doi.org/10.1039/d5na00843c.

Acknowledgements

This study was financially supported by the Faculty of Science, the University Research Council and the Global Excellence and Stature program 4.0, University of Johannesburg.

References

1 M. Kandasamy, S. Sahoo, S. K. Nayak, B. Chakraborty and C. S. Rout, *J. Mater. Chem. A*, 2021, **9**, 17643–17700.
2 I. Shaheen, K. S. Ahmad, C. Zequine, R. K. Gupta, A. G. Thomas and M. A. Malik, *RSC Adv.*, 2021, **11**, 23374–23384.
3 H. Deng, J. Huang, Z. Hu, X. Chen, D. Huang and T. Jin, *ACS Omega*, 2021, **6**, 9426–9432.
4 J. Zhang, M. Gu and X. Chen, *Micro Nano Eng.*, 2023, **21**, 100229.
5 L. Miao, Z. Song, D. Zhu, L. Li, L. Gan and M. Liu, *Mater. Adv.*, 2020, **1**, 945–966.
6 Z. Zhai, L. Zhang, T. Du, B. Ren, Y. Xu, S. Wang, J. Miao and Z. Liu, *Mater. Des.*, 2022, **221**, 111017.
7 C. An, Y. Zhang, H. Guo and Y. Wang, *Nanoscale Adv*, 2019, **1**, 4644–4658.
8 N. Parveen, G. Alsulaim, S. Alsharif, H. Almutairi, H. Alali, S. Ansari and M. Ahmad, *J. Sci.: Adv. Mater. Devices*, 2023, **8**, 100591.
9 S. Ghosh, P. Kumari, C. Saha, H. Singh, I. Waziri, C. Mbileni-Morema and K. Mallick, *ChemistrySelect*, 2024, **9**, e202402255.
10 D. Majumdar, T. Maiyalagan and Z. Jiang, *ChemElectroChem*, 2019, **6**, 4343–4372.
11 S. A. Beknalkar, A. M. Teli, N. S. Harale, D. S. Patil, J. R. Sutar, J. C. Shin and P. S. Patil, *Chin. J. Phys.*, 2021, **72**, 145–158.
12 R. Nare, S. Ramesh, P. Basavi, V. Kakani, C. Bathula, H. Yadav, P. Dhanapal, R. Kotanka and V. Visweswara Rao Pasupuleti, *Sci. Rep.*, 2022, **12**, 1998.
13 S. G. Sayyed, A. V. Shaikh, U. P. Shinde, P. Hiremath and N. Naik, *J. Mater. Sci.: Mater. Electron.*, 2023, **34**, 1361.
14 S. Kasap, I. I. Kaya, S. Repp and E. Erdem, *Nanoscale Adv*, 2019, **1**, 2586–2597.
15 I. Shafi, E. Liang and B. Li, *J. Alloys Compd.*, 2021, **851**, 156046.
16 P.-Y. Tai, M. Sakthivel, Y.-J. Peng, S. Kubendhiran, L.-Y. Lin and K.-C. Ho, *ACS Appl. Energy Mater.*, 2025, **8**, 4122–4133.
17 W. Teng, H. Chen, F. Yu, X. S. Zhao and H. Wang, *Energy Storage Mater.*, 2018, **16**, 545–573.
18 D. Combs, B. Godsel, J. Pohlman-Zordan, A. Huff, J. King, R. Richter and P. F. Smith, *RSC Adv.*, 2021, **11**, 39523–39533.
19 S. Guo, G. Fang, S. Liang, M. Chen, X. Wu and J. Zhou, *Acta Mater.*, 2019, **180**, 51–59.
20 A. Safartoobi, J. Mazloom and F. E. Ghodsi, *J. Energy Storage*, 2023, **68**, 107818.
21 J. J. William, S. Balakrishnan, M. Murugesan, M. Gopalan, A. J. Britten and M. Mkandawire, *Mater. Adv.*, 2022, **3**, 8288–8297.
22 D. Xu, B. Cheng, S. Cao and J. Yu, *Appl. Catal. B: Environ.*, 2015, **164**, 380–388.
23 J. Shen, Y. Lu, J.-K. Liu and X.-H. Yang, *J. Exp. Nanosci.*, 2015, **11**, 1–10.
24 L. Shi, L. Liang, F. Wang, M. Liu and J. Sun, *Dalton Trans.*, 2016, **45**, 5815–5824.
25 N. Gorouhi, M. Haghighi, M. Shabani and C. Almasi, *J. Clean. Prod.*, 2024, **450**, 141850.
26 M. L. Hackert and R. A. Jacobson, *J. Solid State Chem.*, 1971, **3**, 364–368.
27 S. K. Ghosh, H. Singh and K. Mallick, *Emergent Mater*, 2024, **7**, 235–245.
28 M. C. Biesinger, C. Brown, J. R. Mycroft, R. D. Davidson and N. S. McIntyre, *Surf. Interface Anal.*, 2004, **36**, 1550–1563.
29 W. Li, C. Jinfen, G. Rongting, J. Wu, X. Zhou and J. Luo, *J. Mater. Sci.: Mater. Electron.*, 2017, **28**, 14069–14078.
30 Y. Shang, X. Chen, W. Liu, P. Tan, H. Chen, L. Wu, C. Ma, X. Xiong and J. Pan, *Appl. Catal. B: Environ.*, 2017, **204**, 78–88.
31 J. lu, Y. Wang, F. Liu, L. Zhang and S. Chai, *Appl. Surf. Sci.*, 2017, **393**, 180–190.
32 M. P. Shilpa, S. J. Shetty, S. Surabhi, J.-R. Jeong, D. V. Morales, M. S. Murari, V. S. Bhat, S. R. Inamdar, Ravikirana and S. C. Gurumurthy, *J. Mater. Sci.: Mater. Electron.*, 2024, **35**, 860.
33 Y. Wang, L. Yuexin, H. Wang, W. Liu, Y. Li, J. Zhang, H. Hou and J. Yang, *ACS Appl. Energy Mater.*, 2019, **2**, 2063–2071.
34 K. Seevakan, D. Ayyar, P. Devendran, Y. Slimani, A. Baykal and A. Thangavel, *J. Magn. Magn. Mater.*, 2019, **486**, 165254.
35 S. Nagamuthu and K.-S. Ryu, *Sci. Rep.*, 2019, **9**, 4864.
36 B. Yao, S. Chandrasekaran, H. Zhang, A. Ma, J. Kang, L. Zhang, X. Lu, F. Qian, C. Zhu, E. B. Duoss,

C. M. Spadaccini, M. A. Worsley and Y. Li, *Adv. Mater.*, 2020, **32**, 1906652.
37 D. Malko, T. Lopes, E. A. Ticianelli and A. Kucernak, *J. Power Sources*, 2016, **323**, 189–200.
38 W. Kang, X. Kong, J. Li, P. Wang, Y. Sun, X. Zhang, H. Yang and B. Lin, *Mater. Today Energy*, 2020, **18**, 100549.
39 F. Lyu, Y. Bai, Q. Wang, L. Wang, X. Zhang and Y. Yin, *Dalton Trans.*, 2017, **46**, 10545–10548.
40 U. N. Kumar, R. Naik, S. Ghosh, K. Ramanujam and T. Thomas, *Batter. Supercaps*, 2020, **3**, 780–788.
41 A. Farisabadi, M. Moradi, S. Borhani, S. Hajati, M. A. Kiani and A. Tayebi, *J. Mater. Sci.: Mater. Electron.*, 2018, **29**, 8421–8430.
42 S. Sadavar, N. Padalkar, R. Shinde, S. Kochuveedu, U. Patil, A. Patil, R. Bulakhe, C. D. Lokhande, R. Salunkhe and J. L. Gunjakar, *J. Power Sources*, 2022, **524**, 231065.
43 P. R. Deshmukh, Y. Sohn and W. Shin, *Electrochim. Acta*, 2018, **285**, 381–392.
44 Z. Chen, H. Deng, M. Zhang, Z. Yang, D. Hu, Y. Wang and K. Yan, *Nanoscale Adv*, 2020, **2**, 2099–2105.
45 S. Junied Arbaz, A. Mule, M. Nagaraju, A. Kurakula and J. Yu, *Adv. Compos. Hybrid Mater.*, 2025, **8**, 276.
46 S. Kumar, S. T and G. Harichandran, *J. Energy Storage*, 2024, **77**, 110011.
47 T. Li, Z. Liu, L. Zhu, F. Dai, L. Hu, L. Zhang, Z. Wen and Y. Wu, *J. Mater. Sci.*, 2018, **53**, 16458–16465.
48 I. Manohara Babu, M. Sureshkumar, R. M. Rajeshkumar and I. Rathinamala, *J. Alloys Compd.*, 2025, **1010**, 177472.
49 M. Girirajan, G. Seethalakshmi, V. Devi, V. Lm, M. Prabhu, K. Kumar and S. Sudhahar, *Curr. Appl. Phys.*, 2022, **36**, 12299–12309.
50 M. Sharma, R. Adalati, A. Kumar, V. Chawla and R. Chandra, *Appl. Surf. Sci.*, 2021, **555**, 149721.
51 T. Brezesinski, J. Wang, S. H. Tolbert and B. Dunn, *Nat. Mater.*, 2010, **9**, 146–151.
52 D. Gandla, F. Zhang and D. Q. Tan, *ACS Omega*, 2022, **7**, 7190–7198.
53 M. N. Rantho, M. J. Madito, F. O. Ochai-Ejeh and N. Manyala, *Electrochim. Acta*, 2018, **260**, 11–23.
54 H. L. F. Canque, *Analog Electronics Applications: Fundamentals of Design and Analysis*, CRC press, 2016, p. 432, ISBN: 9781315371252.
55 A. S. Sedra and K. C. Smith, *Microelectronic Circuits*, Oxford University Press, 7th edn, 2014, p. 1488, ISBN: 9780199339136.